Final Technical Report

DOE award number: DE-SC0005520

Name of Recipient: Georgia Tech Research Corporation

Project title: Mineral solubility and free energy controls on microbial reaction kinetics: Application to contaminant transport in the subsurface

PI: Martial Taillefert, School of Earth and Atmospheric Sciences, Georgia Institute of Technology, Atlanta GA 30332-0340

Co-PI: Philippe Van Cappellen, Department of Earth and Environmental Sciences, University of Waterloo, Waterloo Ontario, N2L 3G1 (Canada)

Executive Summary

Recent developments in the theoretical treatment of geomicrobial reaction processes have resulted in the formulation of kinetic models that directly link the rates of microbial respiration and growth to the corresponding thermodynamic driving forces (Jin and Bethke, 2003; Dale et al., 2006). The overall objective of this project was to verify and calibrate these kinetic models for the microbial reduction of uranyl (U(VI)) in geochemical conditions that mimic as much as possible field conditions. The approach combined modeling of bacterial processes using new bioenergetic rate laws, laboratory experiments to determine the bioavailability of uranium during uranium bioreduction, evaluation of microbial growth yield under energy-limited conditions using bioreactor experiments, competition experiments between metabolic processes in environmentally relevant conditions, and model applications at the field scale. The new kinetic descriptions of microbial U(VI) and Fe(III) reduction should replace those currently used in reactive transport models that couple catabolic energy generation and growth of microbial populations to the rates of biogeochemical redox processes (e.g. Li et al, 2009). This work was carried out in collaboration between the groups of Taillefert (batch reactor experiments and reaction modeling) at Georgia Tech and Van Cappellen (retentostat experiments and reactive transport modeling) at University of Waterloo (Canada). This project has resulted in the following main findings:

(1) New kinetic rate laws that include bioenergetics were developed to mimic the kinetics of uranium, nitrate, and iron reduction in a variety of natural and biostimulated conditions. These rate laws include the thermodynamic drive of the reactions and microbial growth yields that vary as a function of time to accommodate growth in low energetic conditions. These rate laws can also be coupled to equilibrium calculations to evaluate the speciation of the system as it evolves during the course of reactions.

(2) A reaction kinetic model coupled to equilibrium calculations revealed that the bioavailable uranium species to *Shewanella putrefaciens*, a model metal-reducing microorganism, consist of the low concentrated U(VI) hydroxide complexes mainly and not the most concentrated carbonate complexes which cannot be reduced by *S. putrefaciens*. U(VI) bioreduction rates are enhanced if the geochemical conditions result in an increase in the concentration of these non-carbonated species either as a result of low pH conditions or in the presence of low carbonate concentrations. If the concentration of the uranyl hydroxide complexes is too high, however, the bioavailable species appear toxic to *S. putrefaciens*. These findings suggest that reactive transport models should consider the speciation of uranium to predict the fate of uranium in contaminated

subsurfaces.

(3) The new rate law for U(VI) bioreduction was used to predict the rate of U(VI) bioreduction in the range of pHs found at the three main DOE contaminated sites (Rifle, Hanford, and Oak Ridge). The model predicts that the pH of Hanford falls in the right range to promote U(VI) bioreduction, whereas the pH of Rifle groundwater should be raised slightly to promote bioreduction. Finally, as most metal-reducing bacteria are naturally inhibited under low pH conditions, uranium bioreduction does not appear feasible in the most contaminated zones of the Oak Ridge site where the groundwater is highly acidic (pH 3.5) due to the presence of nitric acid in spent uranium wastes.

(4) The competition between uranium and Fe(III) oxides as terminal electron acceptors by *S. putrefaciens* was investigated to incorporate this competition in the reaction networks of mathematical models. These experiments revealed that in appropriate geochemical conditions, both ferrihydrite reduction and microbial U(VI) reduction may occur simultaneously as both are favorable terminal electron acceptors. In other geochemical conditions, however, U(VI) bioreduction may be inhibited by the respiration of ferrihydrite by a yet to be identified process. In addition, the secondary mineralization of ferrihydrite into more crystalline phases plays an important role in determining the extent of this inhibition, as remineralization to goethite allowed U(VI) bioreduction to proceed after a few days. Finally, the presence of U(VI) also affected the remineralization of ferrihydrite during respiration whether U(VI) reduction was inhibited or not, suggesting that modeling efforts to predict the fate of uranium in subsurface environments should also consider the effect of secondary mineralization on the bioreduction of U(VI) and the effect of U(VI) on the remineralization of Fe(III) oxides.

(5) To accurate reproduce growth rates in energy-limited conditions typically encountered in the field, mathematical models should account for growth yields which couple anabolism to catabolism and act as a feedback to respiration processes. Biogeochemical models that explicitly link variations in growth yield to energy and nutrient availability, however, are expected to provide more flexible simulation tools for geomicrobial reaction systems than microbial growth models based on fixed growth yields. In this study, a new rate law for growth yield based on Gibbs energy dissipation was established and successfully applied to reproduce growth rates of *S. oneidensis* on nitrate in energy-limited conditions. The new bioenergetic rate law was then applied successfully to a field study by coupling growth to the respiration of iron oxides in the presence of acetate by *Geobacter* species in energy-limited and biostimulated conditions.

Summary of results:

(1) Modeling Enzymatic U(VI), Fe(III), and Sulfate Reduction Using Kinetics and Bioenergetics

A mathematical model that includes bioenergetics has been developed to compare the kinetics of uranium and iron reduction. The model follows the kinetics developed previously (Jin and Bethke, 2003) and includes cell biomass, a non-linear term for the electron donor and acceptors, and the thermodynamic driving force, which includes the bioenergetic balance between the Gibbs free energy of the reaction gained by the redox conditions in the system and the Gibbs free energy cost associated with the biochemical machinery, namely the energy required to synthesize ATP. It can easily be shown that if the thermodynamic driving force is not considered in the rate law, the rate calculated is overpredicted at substrate concentrations that are below the thermodynamic limits (**Figure 1**). As most natural conditions include either substrate concentrations or growth conditions that are closed to thermodynamic limits, it is necessary to provide rate laws in these conditions. The model was optimized with the data obtained in the batch reactor and retentostat experiments to determine kinetic parameters in these conditions (see below).

The Gibbs free energy for the respiration of different iron oxides, sulfate, and dissolved uranium species by *Geobacter* and *Shewanella* strains with lactate and acetate as electron donor was determined at different solution concentrations of Fe(II) by-product and sulfate and U(VI) species as terminal electron acceptors (**Figure 2**). These results revealed not surprisingly that the Gibbs free energy of respiration of iron oxides decreases from ferrihydrite to hematite, but also that the reactions with magnetite, goethite, and hematite are at equilibrium ($\Delta G_r = 0$) when approximately 100 μM Fe^{2+} is produced in solution, while ferrihydrite should not reach equilibrium before Fe^{2+} is at about 100 mM. In addition, these results reveal that the Gibbs free energy of the reaction of free uranyl ($UO_2{}^{2+}{}_{(aq)}$) is much more favorable than that of uranyl carbonate species including complexes with calcium, suggesting that carbonate complexes may slow down the rate of reduction of uranium as demonstrated experimentally. Finally sulfate is not as good as an oxidant of acetate and lactate compared to U(VI) species and iron oxides in most experimental conditions as has been shown in field conditions (Istok et al., 2004). These calculations were used to guide the incubations with *Geobacter* and *Shewanella*, as the Gibbs free energy influences respiration rates by affecting the thermodynamic driving force (F_T in Figure 1).

(2) Effect of Uranyl Speciation on the Kinetics of Microbial U(VI) Reduction

Shewanella putrefaciens was incubated in varying concentrations of carbonates, calcium, magnesium, and pH to investigate the role of the speciation of uranyl on uranium respiration rates (**Figure 3**). Results revealed lag phases that correlated inversely with the concentration of calcium and magnesium, possibly reflecting the limiting concentrations of these essential cations in the growth medium. Following the lag phases, uranium bioreduction proceeded at rates highly dependent on the aqueous uranyl speciation. Low pHs prevented uranium bioreduction (Figure 3a), whereas increasing the pH generally increased the rate of uranium bioreduction (Figure 3b). In addition, increasing concentrations of DIC at pH 8.1 resulted in the formation of uranyl carbonates, lower concentrations of uranyl non-carbonate species (i.e., the ‘free’ hydrated uranyl ion, uranyl hydroxides, and other minor uranyl complexes), and slower bioreduction rates (Figure 3c). Similarly, increasing concentration of calcium and magnesium at pH 8.1 decreased bioreduction rates, albeit to different extents (Figure 3d and e). Both thermodynamic and kinetic explanations have been proposed to address the speciation-dependence of uranium bioreduction kinetics (Brooks et al., 2003; Stewart et al., 2011; Ulrich et al., 2011). Thermodynamic considerations, however, cannot explain the drastic changes in uranium bioreduction rates observed, as the differences in energetics due to the speciation of uranium are not high enough to explain these differences. In turn, a speciation-dependent biogeochemical kinetic model that employs the new bioenergetic rate law for the respiration of uranium was able to reproduce all the experiments shown in Figure 3 in a consistent fashion.

In the model, the bioavailability of uranyl non-carbonate species to *S. putrefaciens* explains the dependence of the bioreduction rates on solution composition. Several uranyl non-carbonate species, including the ‘free’ uranyl ion and some of the hydroxide complexes, display redox potentials comparable to the main uranyl carbonate complexes under the experimental conditions (Belli and Taillefert, 2016), despite consistently representing the least abundant species in solution. Simultaneously, the rate constant for the reduction of uranyl non-carbonate species estimated by the model was six orders of magnitude larger than that of the other species (**Figure 4**). Significant differences in bioreduction rate constants among U(VI) species are not unexpected; they are consistent with the recent findings that rate constants for the bioreduction of uranyl hydroxide and organic uranyl species by *Shewanella oneidensis* strain MR-1 are an order of magnitude larger than those determined for uranyl carbonate species and two orders of magnitude larger than Ca uranyl carbonate species (Ulrich et al., 2011). Attributing the bioavailability of U(VI) to uranyl non-carbonate species explains the decrease in bioreduction rates with increasing concentrations of DIC in the pH 8.1 incubations, as well as the more significant deceleration of bioreduction in the presence of Ca^{2+} compared to Mg^{2+} (Figure 3d and e). The apparent inhibition of uranium bioreduction by Ca^{2+} can be attributed to its ability to significantly decrease the concentration of the more bioavailable uranyl non-carbonate species due to the large formation constants of the two calcium uranyl carbonate complexes. Simultaneously, the smaller decrease in bioreduction rate in the presence of Mg^{2+} is explained by the lower formation constant of the single magnesium uranyl carbonate complex (Dong and Brooks, 2006)) and, hence, the smaller decrease in the concentration of uranyl non-carbonate species. Taken together, the kinetic results presented in this study support the hypothesis that the concentration of uranyl non-carbonate species, rather than uranyl carbonate species, controls U(VI) bioreduction rates (Belli et al., 2015).

Regardless of the DIC concentration, uranium bioreduction was negligible in the pH 6.5 incubations (Figure 3a), even though these incubations exhibited the highest concentrations of bioavailable uranyl non-carbonate species (not shown). Similarly, bioreduction rates in the pH 7.5 incubations containing 15 and 30 mM DIC were also lower than expected given the calculated aqueous uranyl speciation (Figure 3b). As the pH does not significantly affect the kinetics of Fe(III) reduction by *S. putrefaciens* between pH 6.5 and 7.5 (Arnold et al., 1986), the metabolic potential of *S. putrefaciens* (i.e., growth and respiration rate) can be assumed to be the same across the range of pH conditions employed in the uranium bioreduction incubations. Thus, changes in U(VI) bioreduction kinetics across different pH and medium compositions used in the current study are attributed to changes in uranyl speciation. As a result, uranium toxicity to *S. putrefaciens* is able to explain the inhibition of bioreduction under geochemical conditions where U(VI) bioavailability is predicted to be the highest. Viability assays confirmed that uranium toxicity to *S. putrefaciens* is also a function of uranyl speciation rather than the total dissolved uranium concentration alone (Belli et al., 2015). In other words, uranium toxicity can be predicted by knowing the aqueous uranyl speciation only, whereas knowledge of the total dissolved uranium concentration alone is not sufficient to predict its toxicity. Taken together, the combined results of the viability assays and bioreduction incubations therefore indicate that uranium toxicity is primarily responsible for the lack of bioreduction in incubations with the highest concentrations of bioavailable uranyl non-carbonate species. The combined effect of bioavailability and toxicity is observed by comparing overall pseudo-first order rate constants k_{obs} to the aqueous speciation of U(VI) at the onset of reduction across all bioreduction conditions (Figure 4b). The k_{obs} for U(VI) bioreduction displays a clear increase with increasing concentration of uranyl non-carbonate species. Above a concentration of approximately 4 nM, however, the rate constant decreases with a further increase in the concentration of uranyl non-carbonate species due to the onset of uranium toxicity. Simultaneously, the largest uncertainties in measured k_{obs} values, which also coincide with the largest discrepancies between measured and modeled k_{obs} values, are found at the onset of uranium toxicity, when U(VI) bioreduction kinetics transitions from being controlled by bioavailability to being controlled by toxicity. In contrast, when represented against the concentration of the uranyl carbonate and ternary uranyl carbonate species, almost all the variability of k_{obs} occurs within a very narrow range of concentration, implying that bioreduction kinetics are largely independent of the concentration of these species. These findings are confirmed by the rate constants predicted by the model for uranyl carbonate and ternary uranyl carbonate species, which are orders of magnitude smaller than the rate constant determined for uranyl non-carbonate species (Figure 4a).

(3) Application of the New Speciation-Dependent Bioenergetic Model to Field Studies

The finding that uranium toxicity is controlled by the concentration of uranyl non-carbonate species, rather than by the concentration of total dissolved uranium, suggests that groundwater composition may affect uranium bioreduction rates even at low total U(VI) concentrations. At the three Department of Energy (DOE) Integrated Field Research Challenge (IFRC) sites, where large-scale bioreduction experiments have been conducted (Hanford, WA; Rifle, CO; and Oak Ridge, TN), distinct waste disposal histories and groundwater compositions affect the implementation of uranium bioreduction as a bioremediation strategy. At all three sites, ternary uranyl carbonate species represent the main fraction of U(VI) above pH 6.5 due to the prevalence of Ca^{2+} and Mg^{2+} (**Figure 5**). At the Hanford site (Figure 5a), a local minimum in bioreduction rate is predicted at pH 8.8, which corresponds to the minimum concentration of bioavailable uranyl non-carbonate species. Below or above this pH, bioreduction rates are predicted to increase, mirroring changes in the concentration of uranyl non-carbonate species. The pH of Hanford groundwater, however, ranges from 7.1 to 8.7 (Zachara et al., 2013) which includes the critical pH window from 7.5 to 8.1 where, according to the model, bioreduction rates decrease abruptly with decreasing pH even as the concentration of bioavailable uranyl non-carbonate species increases. Over this pH range, uranium toxicity apparently overcomes the increase in bioavailability of U(VI) as a result of the increase in concentration of the 'free' uranyl ion (Figure 5a). Under these conditions, bioreduction rates are highly sensitive to pH, and bioreduction may be promoted by a slight increase in pH, which decreases the concentration of the toxic 'free' uranyl ion despite simultaneously decreasing the bioavailability of U(VI). In turn, Rifle groundwater pH varies from 6.6 to 7.4 (Zachara et al., 2013), a range over which bioreduction rates are inhibited by uranium toxicity (Figure 5b). The model therefore predicts that the pH of Rifle groundwater should be raised to promote bioreduction. Although the kinetic model predicts similar trends in bioreduction rate above pH 8 at the Hanford (Figure 5a) and Rifle (Figure 5b) sites, bioreduction rates at Hanford are predicted to be 5 times greater due to the larger concentration of bioavailable uranyl non-carbonate species. Finally, as most metal-reducing bacteria are naturally inhibited under low pH conditions, uranium bioreduction is not feasible in the most contaminated zones of the Oak Ridge site (Figure 5c) where the groundwater is highly acidic (pH 3.5) due to the presence of nitric acid in spent uranium wastes. Correspondingly, substantial treatment of the groundwater was found to be necessary to increase pH, decrease Ca^{2+} concentrations, and promote uranium bioreduction at this site (Wu et al., 2006 and 2007). Interestingly, the model predicts that uranium bioreduction can be extended to a lower pH at the Oak Ridge site (pH 6.8) compared to the Hanford (pH 7.3) and Rifle (pH 7.3) sites due to higher concentrations of DIC, Ca^{2+}, and Mg^{2+} which decrease the toxicity of uranium and promote bioreduction. These results indicate that efforts to increase uranium immobilization via bioreduction by promoting the formation of bioavailable uranyl non-carbonate species may ultimately be limited by the toxicity of uranium to indigenous metal-reducing bacteria.

(4) Geochemical Controls of the Competitive Inhibition of Microbial Uranium Reduction by Iron Oxides

The biogeochemical cycling of uranium is tightly coupled to that of iron due, in part, to the overlapping potentials of the U(VI)/U(IV) and Fe(III)/Fe(II) redox couples (Belli and Taillefert, 2016). Indeed, pure cultures of metal-reducing bacteria are able to simultaneously reduce iron oxides and U(VI) (Frederickson et al., 2000; Stewart et al., 2011; Wielinga et al., 2000), though decreased rates of uranium reduction in the presence of different forms of iron oxides suggest that iron oxides may divert the flux of electrons from U(VI) to Fe(III). In this study, the geochemical controls on the competitive inhibition of dissimilatory U(VI) reduction by ferrihydrite were investigated with pure cultures of *Shewanella putrefaciens*. Experimental conditions were chosen to ensure that ferrihydrite reduction was always thermodynamically favorable, but Gibbs free energy yields of U(VI) bioreduction were manipulated by varying the carbonate alkalinity and pH in the presence of lactate as electron donor. Hence, in the presence of 20 mM DIC at a pH of 8.2, the ΔG_r of U(VI) respiration was 15.5 kJ/mol more favorable than the ΔG_r of ferrihydrite respiration at the onset of microbial respiration, whereas in the presence of 60 mM DIC at a pH of 7.7, the ΔG_r of ferrihydrite respiration was initially 16.4 kJ/mol more favorable than the ΔG_r of U(VI) respiration.

Uranium removal and Fe(II) production by *S. putrefaciens* (**Figure 6**) in incubations conducted at pH 8.2 with both competitive terminal electron acceptors occurred immediately and simultaneously without an apparent lag phase, in contrast to the initial lag phases observed in otherwise identical incubations conducted with U(VI) or ferrihydrite as sole terminal electron acceptor (Figure 6a and c). Near-complete removal of uranium and production of Fe(II) was observed by day 2, after which Fe(II) was produced gradually. Interestingly, the extent of Fe(II) production in the presence of uranium exceeded the ferrihydrite-only treatment by approximately 25% (Figure 6c). In pH 7.7 incubations conducted in the presence of both terminal electron acceptors, the removal of dissolved uranium was not significant before day 2 (Figure 6b), when about 50% of total Fe(II) produced over the entire incubation was generated (Figure 6d). In turn, Fe(II) was produced continuously throughout the incubation to a final concentration of about 4 mM, similar to the ferrihydrite-only treatment under the same geochemical conditions (Figure 6d) but significantly higher than the incubations conducted at pH 8.2 with or without uranium (Figure 6c). The rate and extent of consumption of ascorbate-extractable solid iron in incubations conducted in the presence of both terminal electron acceptors was also decreased compared to the ferrihydrite-only treatment at pH 8.2 (Figure 6e), whereas the rate and extent of consumption of ascorbate-extractable iron in the pH 7.7 incubations were similar regardless of the presence or absence of U(VI) (Figure 6f). Finally, magnetite was the sole mineral product identified in the pH 8.2 incubations with ferrihydrite only, whereas a mixture of siderite and magnetite was identified as the final solid-phase product in the ferrihydrite-only treatment at pH 7.7 (not shown). In turn, the presence of uranium affected the secondary mineralization of ferrihydrite as goethite was identified along with magnetite as final secondary mineral products in pH 8.2 incubations and siderite was the only mineral product identified at pH 7.7 (not shown).

The evolution of U(VI) and Fe(II) produced during the reduction of ferrihydrite was modeled using both respiration reactions coupled to bioenergetics (Figure 1), modified to account for the speciation-dependent rate law for microbial uranium respiration (Belli et al., 2015) as well as the secondary mineralization of ferrihydrite (Eq. (1)) (Boland et al., 2014), the abiotic reduction of U(VI) by adsorbed Fe(II) (Liger et al., 1999) (Eq. (2)), and the abiotic oxidation of U(IV) by-product by ferrihydrite (Ginder-Vogel et al., 2010) (Eq. (3)).

$$r = k_{rm}\frac{[Fe(II)_{ads}]}{[Fe(III)]} \tag{1}$$

$$r = k_{ru}[Fe(II)_{ads}][U(VI)] \tag{2}$$

$$r = k_{rf}[Fe(III)][UO_2(am)] \tag{3}$$

To ensure the modeling exercise consistent, rate parameters for the bioreduction of uranium and ferrihydrite as well as rate constants for the remineralization of ferrihydrite by Fe(II) (Eq. (1)) were first optimized using data from the independent incubations with each electron acceptor conducted in both pH conditions, then maintained constant to reproduce the dual terminal electron acceptor incubations. Using this approach, the data could not be reproduced even when optimizing the kinetic of abiotic reduction of U(VI) by adsorbed Fe(II) (Eq. (2)) or U(IV) oxidation by ferrihydrite (Eq. (3)). These findings suggest that under geochemical conditions favoring the respiration of ferrihydrite compared to U(VI) respiration, *S. putrefaciens* preferentially utilizes ferrihydrite as terminal electron acceptor, thereby diverting electrons from U(VI) and ultimately inhibiting uranium reduction from solution. To test this hypothesis and account for the competition between these two processes, the rate of U(VI) bioreduction was allowed to be inhibited by the presence of ferrihydrite when the Gibbs free energy of reduction of ferrihydrite is more favorable than that of U(VI) bioreduction according to:

$$r_{U(VI)} = [X]\left(\frac{1}{1+\frac{[Fe(III)]}{K_I}}\right)r^{U}_{resp}F_T \tag{4}$$

where $r_{U(VI)}$ is the rate of U(VI) bioreduction [mM hr^{-1}], K_I is the ferrihydrite respiration inhibition constant [mM], [Fe(III)] is the concentration of ferrihydrite [mM], r^{U}_{resp} is the rate of U(VI) bioreduction calculated according to the equation of Figure 1, and F_T is the thermodynamic driving force of the reaction also calculated following the equation of Figure 1. The concentration of the electron donor (lactate) was in excess in these experiments and therefore assumed to display a zero order reaction rate.

The rate law for microbial uranium respiration was able to reproduce time series of uranium removal in uranium-only treatments at both pHs (Figure 6a and b). Similarly, the reaction network proposed for the microbial reduction of ferrihydrite and secondary mineralization products reproduced $Fe(II)_T$ time series in the ferrihydrite-only incubations (Figure 6c and d) and largely reproduced time series of ascorbate-extractable solid-phase iron (Figure 6e and f) and the final solid-phase assemblage under both pHs even though these data were not used to calibrate the model. When the calibrated model was applied to the competitive TEA incubations it was able to capture the stark differences in initial uranium removal rates between the two pH conditions: simultaneous uranium removal and Fe(II) production in the pH 8.2 incubations (Figure 6a and c) and inhibited rates of uranium reduction at the beginning of the pH 7.7 incubations during active production of Fe(II) (Figure 6b and d). The best fit of the model was obtained by minimizing the rate constant of U(IV) oxidation by ferrihydrite and using an inhibition constant concentration of 200 µM ferrihydrite in the uranium bioreduction rate law (Eq. (4)). These findings suggest that the competitive inhibition of microbial U(VI) respiration by ferrihydrite, rather than rapid oxidation of U(IV), is responsible for the slow initial rate of uranium removal in the pH 7.7

incubation with U(VI) and ferrihydrite. In addition, the modeling exercise revealed that the secondary mineralization of ferrihydrite into more crystalline phases plays an important role in determining the extent of this inhibition. Without secondary mineralization, the production of Fe(II) and the removal of ferrihydrite (i.e. ascorbate-iron) could not be reproduced accurately by the model at both pH conditions. More importantly, the low removal rate of ferrihydrite without remineralization in the model allowed inhibition of uranium reduction past day 2 in the pH 7.7 incubations. In contrast, adding remineralization to goethite allowed U(VI) bioreduction to proceed after day 2, as more crystalline Fe(III) oxide phases do not inhibit U(VI) bioreduction in contrast to ferrihydrite (Frederickson et al., 2000; Stewart et al., 2011; Wielinga et al., 2000), simply because the Gibbs free energy gained from the respiration of goethite by *S. putrefaciens* is higher than that of U(VI) bioreduction (**Figure 7**). Finally, dissimilatory U(VI) reduction had a pronounced effect on the final secondary mineralization products of ferrihydrite in both pH conditions. It promoted the formation of goethite and poorly crystallized magnetite at pH 8.2 compared to the formation of well-crystallized magnetite in the presence of ferrihydrite only at that pH. It also prevented the formation of magnetite at pH 7.7 in contrast to the ferrihydrite only incubations. As goethite and magnetite are secondary mineralization products of the same precursor (i.e., ferrihydrite), and as the flux of electrons into the ferrihydrite lattice is the primary determinant of the final secondary mineralization products of ferrihydrite (Hansel et al., 2005), different electron fluxes in the presence and absence of uranium may be responsible for the different secondary mineralization products. *Shewanella* spp. produce organic exopolymer matrices (broadly referred to as extracellular polymeric substances, EPS) which assist in biofilm formation and colonization of mineral surfaces (Neal et al., 2007), and uranium enhances the production of EPS and membrane vesicles, perhaps as a mechanism to deal with encrustation and periplasmic or intracellular precipitation of U(IV) solid phases (Marshall et al., 2006). EPS production and biofilm formation enhances the close spatial association of U(IV) precipitates, cell biomass, and iron solid phases (Belli and Taillefert, 2016), which may occlude ferrihydrite surfaces, decrease the flux of electrons into the ferrihydrite lattice, and thus favor the formation of goethite at pH 8.2 or inhibit secondary mineralization at pH 7.7. Overall, these incubations reveal that modeling efforts to model the fate of uranium in subsurface environments should also consider the effect of secondary mineralization on the bioreduction of U(VI) and the effect of U(VI) on the remineralization of Fe(III) oxides.

(5) Predicting Microbial Growth Yields Under Energy-Limited and Biostimulated Conditions

The growth yield (*Y*) forms the stoichiometric link between anabolism to catabolism and is defined as the portion of the growth substrate consumed that is converted into cellular biomass (Lipson, 2015); it is expressed in, for instance, grams of cells per mol of substrate (e.g., Strohm et al., 2007) or C-mol biomass per C-mol substrate (e.g. Rutgers et al., 1989). Biogeochemical models that explicitly link variations in *Y* to energy and nutrient availability are expected to provide more flexible simulation tools for geomicrobial reaction systems than microbial growth models based on fixed *Y* values (e.g. Long et al., 2016; Reed et al., 2014). Under energy-limited conditions, *Y* can be related to the catabolic energy yield via empirical relationships (e.g., Roden and Jin, 2011) or through bioenergetically based models (Heijnen et al., 1992; McCarty, 2007).

Models grounded in thermodynamics provide a theoretically sound approach to predict *Y* values. Moreover, the experimental determinations of *Y* values when solid phase electron acceptors (or reaction products) are involved may be difficult, for example during dissimilatory reduction of insoluble iron(III) oxyhydroxides or the production of uraninite during uranyl reduction, because the solids interfere with commonly used optical methods to measure biomass. In these cases, predictive bioenergetic models offer an alternative method to estimate metabolism-specific *Y* values. Most existing bioenergetic models, however, have been calibrated with data from bioengineering and biotechnological applications that may not provide realistic analogues for the low energy-yielding metabolisms prevailing in many subsurface environments. To evaluate the current bioenergetic-based methods to predict microbial growth and their potential application to natural systems, an extensive review and critical assessment of current models used to predict static *Y*, namely the thermodynamic electron equivalents (TEEM) (McCarty, 2007), linear free energy relationship (LFER) (Roden and Jin, 2011), and Gibbs energy dissipation (GEDM) (Heijnen et al., 1992) methods, were conducted. The accuracy of the models to predict *Y* was evaluated using a compilation of 141 literature *Y* values of the major metabolic pathways expected to dominate organic matter degradation in the subsurface (**Figures 8**) and were comprised of predominantly (~58%) low energy (< 25 kJ (mol e^-)$^{-1}$) metabolisms (**Figure 9**). The results indicate that GEDM yields the lowest overall relative error (30%) compared to TEEM (38%) and LFER (58%). The higher accuracy of GEDM over the more commonly used TEEM is even more pronounced for the lower energy metabolisms which yield relative errors of 34% (GEDM) and 46% (TEEM) (**Figure 10**). In addition, predicting *Y* using Gibbs energies calculated under non-standard conditions, rather than imposing biochemical standard conditions, improves accuracy by 18% for low-energy metabolisms. Interestingly, the lowest reported *Y* values are for U(VI) reduction which is likely due to energy "spilling' in response to uranium toxicity (Belli et al., 2015), as observed previously for microbial growth yields in the presence of Cu, Ni and Zn (Cabrero et al., 1998; Gökçay and Yetis, 1996). This finding highlights the need to better constrain the energy spilled during uranyl reduction for use in bioenergetic-based reactive transport models.

Based upon the comparison across *Y* prediction models, a bioenergetic-based GEDM model was developed to predict dynamic microbial growth in the subsurface under both natural and biostimulated conditions. The dynamic Y model builds upon previous models (Heijnen, 1999; Pirt, 1965) and accounts for temporal changes in the Gibbs energy of catabolism gained, dissipated and used for maintenance:

$$r_x = (r_e - m_e X_t)\frac{1}{\Delta G^{max}_{Diss/r_x}} \tag{5}$$

where r_x [C-mol biomass (L h)$^{-1}$] is the biomass production rate; m_e [kJ (C-mol biomass h)$^{-1}$] is the microbial maintenance energy rate or the amount of energy that is devoted to all non-growth related functions, determined experimentally or calculated using an empirical formula (Tijhuis et al. 1993); $\Delta G^{max}_{Diss/r_x}$ is the maximum amount of energy dissipated [kJ (C-mol biomass)$^{-1}$] or the total Gibbs energy required to build 1 C-mol of biomass in the absence of maintenance energy, calculated using the Gibbs energy of the metabolic reaction derived from the maximum growth yield (Y^{max}) determined experimentally using chemostats; and r_e is the energy supply rate [kJ (L·h)$^{-1}$] calculated from the rate of consumption of the energy-limiting substrate (r_s) and the Gibbs energy of catabolism (ΔG_{cat}) under non-standard conditions:

$$r_e = r_s \cdot \Delta G_{cat} \tag{6}$$

The predicted observed yield [C-mol biomass $(kJ)^{-1}$] at each time step is then determined from:

$$Y(t) = \frac{r_x}{r_e} \tag{7}$$

and the integrated form of Eq. (5) calculates biomass concentration (X) at each time step (t) as a function of energy consumption:

$$X(t) = \frac{r_e}{m_s} + \left[X_0 - \left(\frac{r_e}{m_e}\right)\right]\exp\left(-\frac{1}{\Delta G^{max}_{Diss/r_x}} m_e t\right) \tag{8}$$

(6) Reproducing Microbial Growth in the Subsurface Under Low Energy Conditions Using a Retentostat

In low energy environments such as subsurface ecosystems, the minimum energy required to sustain cellular integrity and function (i.e., maintenance energy) represents a significant portion of the total energy available to microbial communities. To further elucidate the bioenergetic controls on microbial growth in the subsurface, a low energy environment was reproduced in the laboratory using a flow through bioreactor system (i.e., retentostat). Experiments were designed to determine the maintenance energy requirement and maximum growth yield (Y^{max}) of the model bacterium *Shewanella oneidensis*. It was hypothesized that *S.oneidensis* would direct most of its catabolic energy to maintenance and energy dissipation, rather than growth under the energy-limited conditions imposed by the retentostat, thereby invoking the survival strategy of typical subsurface microorganisms which combines optimal energy generation, near-zero growth rates and long life spans.

An existing bioreactor system (Applikon EZ-control®, 2.4 L) was modified to include a biomass retention filtration unit (retentostat) which results in biomass accumulation over time (**Figure 11**). An artificial low-nutrient groundwater medium based on groundwater concentrations of major and minor cations and anions collected from the Old Rifle DOE site was optimized for slow *S. oneidensis* growth and was supplied and removed from the reactor at flow rates on the order of 1 mL min^{-1} with a dilution rate of 0.025 h^{-1}. The retentostat was run under electron acceptor limited conditions with nitrate, a common groundwater contaminant, supplied at 17.5 $\mu M\ h^{-1}$ and lactate supplied in excess at 125 $\mu M\ h^{-1}$. Respiratory ammonification of nitrate by *S. oneidensis* and cell growth was monitored over time (35 days) and showed a slow yet increasing microbial growth over time (generation time = 17 days) (**Figure 12**). A maintenance energy demand was estimated (2.4 kJ C-mol biomass h^{-1}) by fitting the biomass production rates to Eq. (8). The maintenance energy demand of *S. oneidensis* was similar to typical low-energy metabolism maintenance energies reported in the literature (~3 kJ C-mol biomass h^{-1}). Results also showed that under-low energy conditions *Shewanella oneidensis* devotes most of its catabolic energy to maintenance and dissipation with little growth. The relatively high loss of energy via dissipation is a direct consequence of the 2nd Law of Thermodynamics, which sets an absolute limit to the microbial activity in the subsurface. These experiments also demonstrate that the bioenergetic-based GEDM model can be used in the laboratory with retentostats to extract bioenergetic parameters for use in biomass-explicit models at the field scale.

Gibbs free energy yields were manipulated by varying the concentrations of U(VI) and electron donor, as well as the carbonate alkalinity, pH, and calcium and magnesium concentrations. Bacteria were also supplied with both U(VI) and different iron(III) oxyhydroxides. The objective of this part of the project was to determine how geochemical conditions controls the competition between microbial U(VI) and Fe(III) reduction. The data were used to derive the functional dependencies of enzymatic U(VI) and Fe(III) reduction kinetics on the corresponding Gibbs energies of reaction.

(7) New Growth Model Application at the Field Scale

The new growth model was validated at the field scale using previously published in situ cell counts of *Geobacter* sp. collected during a biostimulation event at the Rifle, Colorado field site (Holmes et al., 2013). Moreover, we also used an average natural acetate turnover rate previously reported for the Rifle field site by Zhuang et al. (2011) to simulate microbial growth under natural conditions. It was assumed that the catabolic energy consumed for growth and maintenance was due to acetate oxidation coupled to goethite reduction according to:

$$8FeOOH + C_2H_3O_2^- + 15H^+ \rightarrow 8Fe^{2+} + 2HCO_3^- + 12H_2O \tag{9}$$

Published groundwater concentrations (Bao et al., 2014; Holmes et al., 2013) under natural and biostimulated conditions were converted to activities using PHREEQC based on a groundwater temperature of 12°C (Arora et al., 2016). The simulation was run for 35 days to replicate the experimental time frame used by Holmes et al. (2013) and the model output was converted to cell numbers by assuming a cell weight of 1 pg per *Geobacter* cell (Zhuang et al., 2011) for easy comparison to literature cells counts. As shown in **Figure 13**, the model output is in good agreement with *Geobacter sp.* cell numbers and falls within the error bars of the cell enumeration method. As expected, the predicted biomass growth under natural conditions is negligible (Figure 13) and is much lower as compared to growth under biostimulated conditions. Overall, this new bioenergetic-based growth model may help improve the simulation of microbially-mediated reaction networks in reaction transport models under the fluctuating catabolic energy supply conditions typical of many natural environments.

References:

Arnold, R. G.; DiChristina, T. J.; Hoffmann, M. R. (1986) *Appl. Environ. Microbiol.* **52**, 281-289.

Arora, B. et al. (2016) *Biogeochem.* **127**, 367-396.

Belli, K.; DiChristina, T.J.; Van Cappellen, P.; Taillefert, M. (2015) *Geochim. Cosmochim. Acta* **157**, 109-124.

Belli, K.; Taillefert, M. (2016) In: Rinklebe, J., Knox, A.S., Paller, M. (Eds.), Trace elements in waterlogged soils and sediments. CRC Press, a Taylor & Francis Company, pp. 185-223.

Boland, D. D. et al. (2014) *Environ. Sci. Technol.* **48**, 5477-5485.

Brooks, S. C. et al. (2003) *Environ. Sci. Technol.* **37**, 1850-1858.

Cabrero, A.; Fernandez, S.; Mirada, F.; Garcia, J. (1998) *Wat. Res.* **32**, 1355-1362.

Dale, A.W.; Regnier, P.; Van Cappellen, P. (2006) *Amer. J. Sci.* **306**, 246-294.

Dong, W.; Brooks, S. C. (2006) *Environ. Sci. Technol.* **40**, 4689-4695.

Frederickson, J. K. et al. (2000) *Geochim. Cosmochim. Acta* **64**, 3085-3098.

Ginder-Vogel, M. A.; Stewart, B.; Fendorf, S. (2010) *Environ. Sci. Technol.* **44**, 163-169.

Gökcay, C. F.; Yetis, U. (1996) *Wat. Sci. Technol.* **34**, 163-171.

Hansel, C. M.; Benner, S. G.; Fendorf, S. (2005) *Environ. Sci. Technol.* **39**, 7147-7153.

Heijnen, J. J.; van Loosdrecht, M. C. M.; Tijhuis, L. (1992) *Biotechnol. Bioeng.* **40**, 1139-1154.

Heijnen, J. J.; Kleerebezem, R.; Flickinger, M. C. (2009) In *Encyclopedia of Industrial Biotechnology*, John Wiley & Sons, pp 1-66.

Holmes, D. E. et al. (2013). *Appl. Environ. Microbiol.* **79**, 1646-1653.

Jin, Q. and Bethke, C.M. (2005) *Geochim. Cosmochim. Acta* **69**, 1133-1143.

Istok, J. D. et al. 2004. *Environ. Sci. Technol.* **38**, 468-475.

Li, L. et al. (2009) *Environ. Sci. Technol.* **43**, 5429-5435.

Liger, E.; Charlet, L.; Van Cappellen, P. (1999) *Geochim. Cosmochim. Acta* **63**, 2939-2955.

Lipson, D. A. (2015) *Front. Microbiol.* **6**, 615-621.

Long, P. E.; Williams, K. H.; Hubbard, S. S.; Banfield, J. F. (2016) *Trends Microbiol.* **24**, 600-610.

Marshall, M. J. et al. (2006) *PlOS Biol.* **4**, 1324-1333.

McCarty, P. L. (2007) *Biotechnol. Bioeng.* **7**, 377-388.

Neal, A. L. et al. (2007) *Biomacromol.* **8**, 166-174.

Pirt, S. J. (1965) *Proc. Royal Soc. Lond. B, Biol. Sci.* **163**, 224-231.

Reed, D. C.; Algar, C. K.; Huber, J. A.; Dick, G. J. (2014) *Proc. Nat. Acad. Sci.* **111**, 1879-1884.

Regnier, P. et al. (2005) In *Reactive Transport in Soil and Groundwater: Processes and Models*, Nuetzmann, G.; Viotti, P.; Aagaard, P., Eds. Springer-Verlag: Berlin, pp 107-126.

Roden, E. E.; Jin, Q. S. (2011) *Appl. Environ. Microbiol.* **77**, 1907-1909.

Rutgers, M.; van der Gulden, H. M. L.; Dam, K. (1989) *Biochim. Biophys. Acta* **973**, 302-307.

Stewart, B. D.; Amos, R. T.; Nico, P. S.; Fendorf, S. (2011) *Geomicrobiol. J.* **28**, 444-456.

Strohm, T. O.; Griffin, B.; Zumft, W. G.; Schink, B. (2007) *Appl. Environ. Microbiol.* **73**, 1420-1424.

Tijhuis, L.; Van Loosdrecht, M. C. M.; Heijnen, J. J., (1993) *Biotechnol. Bioeng.* **42**, 509-519.

Ulrich, K.-U.; Veeramani, H.; Bernier-Latmani, R.; Giammar, D. E. (2011). *Geomicrobiol. J.* **28**, 396-409.

Wielinga, B. et al. (2000) *Environ. Sci. Technol.* **34**, 2190-2195.

Wu, W. et al. (2006) *Environ. Sci. Technol.* **40**, 3986-3995.

Wu, W. et al. (2007) *Environ. Sci. Technol.* **41**, 5716-5723.

Zachara, J. M. et al. (2013) *J. Contam. Hydrol.* **147**, 45-72.

Zhuang, K. et al. (2011) *ISME J.* **5**, 305-316.

Products Developed under the Award:

Publications:

Belli K.M., Saad E., Tang Y., DiChristina T.J., Taillefert. M. (2016) Geochemical controls of the competitive inhibition of microbial uranium reduction by iron oxides. In review.

Smeaton, C.M., Van Cappellen, P. (2016). Predicting microbial growth yields under energy-limiting conditions: A critical assessment. In review.

Bajracharya, B., Smeaton, C.M., Markelov, I. Markelova, E., Lu, C., Cirpka, O., Van Cappellen, P. (2016) Anaerobic degradation of organic matter in energy-limited environments – A bioenergetic modeling approach. In review.

Stolpovsky K., Fetzer I., Van Cappellen P., Thullner M. (2016) Influence of dormancy on microbial competition under intermittent substrate supply: Insights from model simulations. *FEMS Microbiology Ecology*, 92.

Belli, K.M., Taillefert, M., 2016. Biogeochemical Processes Regulating the Mobility of Uranium in Sediments; *Trace Elements in Waterlogged Soils and Sediments*. CRC Press, pp. 185-223.

Couture, R.-M., Charlet, L., Markelova, E., Madé, B., Parsons, C.T. (2015). On-off mobilization of contaminants in soils during redox oscillations. *Environmental Science &*

Technology, 49, 3015-3023.

Belli K., DiChristina T.J., Van Cappellen P., Taillefert M. (2015) The effect of uranyl speciation on the kinetics of microbial uranium reduction. *Geochim. Cosmochim. Acta* 157, 109-124.

Alexandratos, V.G., Behrends, T., Van Cappellen, P. (2014) Sulfidization of lepidocrocite and its effect on uranium phase distribution and reduction. *Geochim. Cosmochim. Acta* 142, 570-586.

Salome K.R., Green S.J., Beazley M.J., Webb S.M., Kostka J.E., Taillefert M. (2013) The role of anaerobic respiration in the immobilization of uranium through biomineralization of phosphate minerals. *Geochim. cosmochim. Acta.* 106, 344-363.

T. Borch, R. Kretzschmar, A. Kappler, P. Van Cappellen, M. Ginder-Vogel, A. Voegelin, K. Campbell (2010). Biogeochemical redox processes and their impact on contaminant dynamics. *Environmental Science & Technology* 44, 15-23.

<u>Abstracts and Presentations</u>:

K. M. Belli, T. J DiChristina, P. Van Cappellen, M. Taillefert. 2016. Geochemical controls of competitive inhibition of microbial uranium reduction by iron oxides. Goldschmidt Conference, Yokohama (Japan).

M. Taillefert. 2015. Effect of uranium toxicity on the immobilization of uranium by subsurface microorganisms. Invited Talk. 250th ACS National Meeting, Boston, Massachusetts.

P. Van Cappellen, C.M. Smeaton. 2015. Are microbes better at thermodynamics than geochemists? Plenary Lecture. Goldschmidt, Prague (Czech Republic).

C.M. Smeaton, B. Bajracharya, C. Ridenour, P. Van Cappellen. 2015. Bioenergetic limitations on slow microbial growth in the subsurface: What is the burden of maintenance on the overall energy budget? Joint AGU-GAC-MAC-CGU Assembly, Montreal (Canada).

K. M. Belli, T. J. DiChristina, P. Van Cappellen, M. Taillefert. 2015. Differentiating kinetic and thermodynamic controls of microbial uranium reduction in the presence of iron oxides. 249th ACS National Meeting, Denver, CO.

K. M. Belli, T. J. DiChristina, P. Van Cappellen, M. Taillefert. 2013. Effect of pH-driven changes in U(VI) speciation on U(VI) bioreduction rates by *Shewanella putrefaciens*. 245th National American Chemical Society Meeting, New Orleans, LA.

K. Belli, P. Van Cappellen, T. J. DiChristina, M. Taillefert. 2012. Characterizing the biological mechanism of uranium reduction using novel voltammetric techniques. Subsurface Biogeochemical Research (SBR). PI Meeting, Washington, DC.

M. Taillefert. 2012. Biomineralization and bioreduction of U(VI) as bioremediation strategies: Insights from speciation and kinetic studies. Uranium Biogeochemistry Workshop, Monte Verita, Ascona, Switzerland.

P. Van Cappellen. 2012. Elemental biogeochemical cycles in subsurface environments. Subsurface Biogeochemical Research (SBR). PI Meeting, Washington, DC.

K. Belli, L. Pastor, N. Szeinbaum, P. Van Cappellen, M. Taillefert (2011) Influence of uranyl speciation on uranium reduction by metal-reducing bacteria, 242nd American Chemical Society National Meeting, Denver (CO).

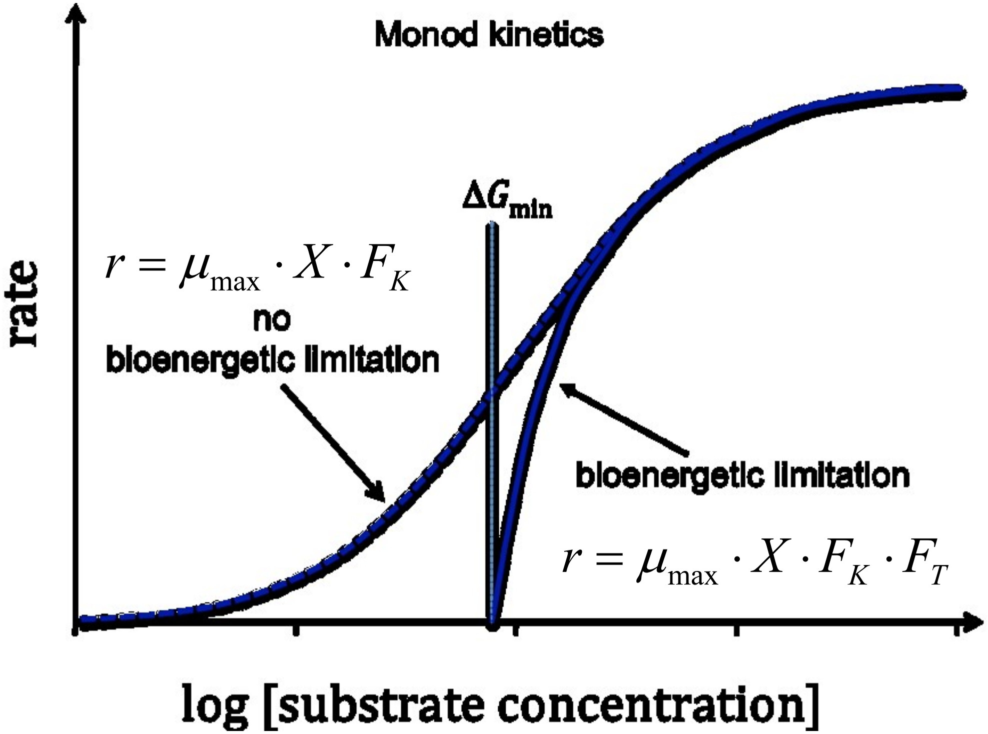

$$F_K = \frac{\left[\mathrm{UO_2^{2+}}\right]}{K_{\mathrm{UO_2^{2+}}} + \left[\mathrm{UO_2^{2+}}\right]} \cdot \frac{\left[\mathrm{Lac^-}\right]}{K_{\mathrm{Lac^-}} + \left[\mathrm{Lac^-}\right]}$$

$$F_T = 1 - \exp\left(\frac{\Delta G_r + m\Delta G_{\mathrm{ATP}}}{\chi RT}\right)$$

Figure 1. Schematic diagram illustrating the effect of the bioenergetics on the rate of a microbial reaction (r) as a function of the substrate concentration (here U(VI)). The dashed line represents the case, where bioenergetics is not considered in the rate law (i.e. simple Michaelis Menten kinetics). The plain line considers the thermodynamic driving force, F_T, which considers the balance between energy gained during the redox reaction (ΔG_r) and the energy cost for the synthesis of ATP (ΔG_{ATP}). ΔG_{min} corresponds to the substrate concentration at which the Gibbs energy of reaction equals the minimum Gibbs energy required for ATP synthesis. At high substrate concentrations (i.e. far from equilibrium), thermodynamic limitation vanishes ($F_T = 1$), and the rate reaches a maximum value. At substrate concentrations near or below the thermodynamic limit, however, the rate of microbial reduction is overpredicted if the bioenergetic limitations are not considered. As most natural conditions include either substrate concentrations or growth conditions that are closed to thermodynamic limits, it is necessary to provide rate laws in these conditions (From Regnier et al., 2005.)

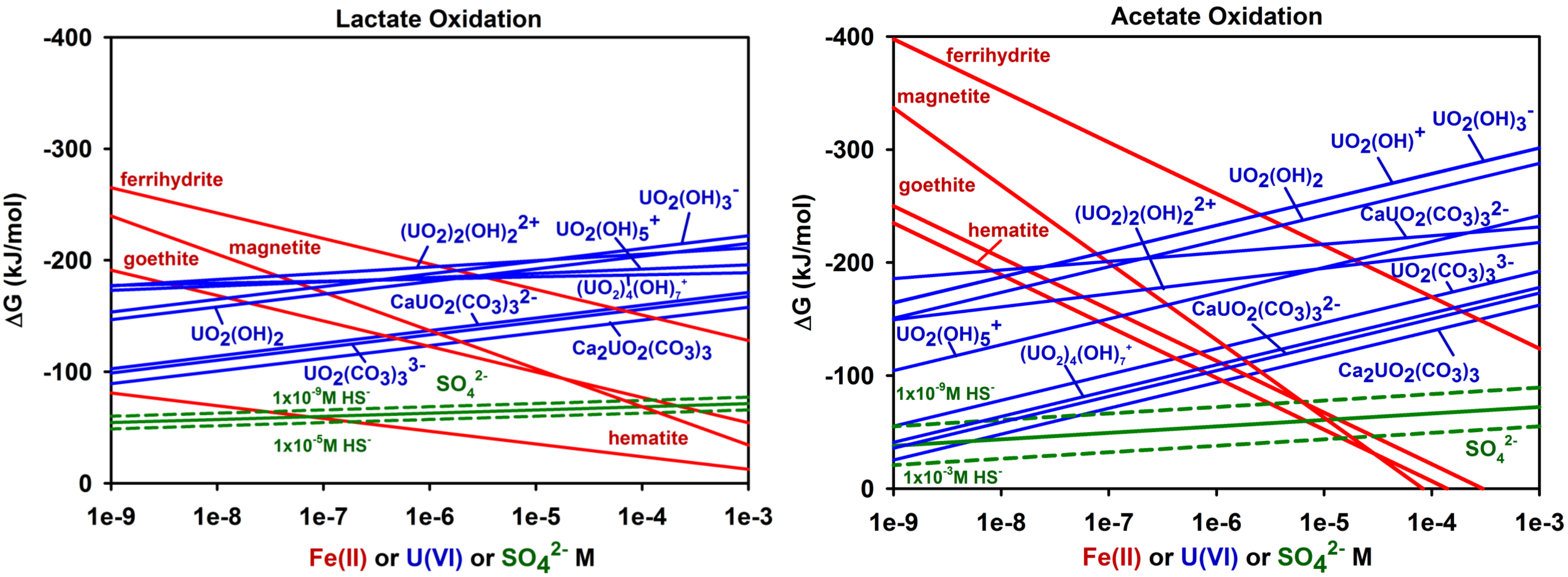

Figure 2. Gibbs free energy change of the reaction of different iron oxides (red), sulfate (green), and uranium species (blue) as a function of the concentration of Fe(II) product, and U(VI) and SO_4^{2-} reactants with A. lactate and B. acetate as electron donor for anaerobic respiration by *Shewanella* and *Geobacter* species, respectively. Concentrations used to calculate ΔG_r: HCO_3- = 7.7 mM; Acetate = 1 mM; Lactate = 1 mM; Ca^{2+} = 4.8 mM; pH 7.5. These calculations reveal that respiration of uranium is always more favorable than sulfate reduction and may be more favorable than respiration of iron oxides if [U(VI)] > 10 μM in these environmental conditions. In addition, lactate oxidation is more favorable with uranyl hydroxide than carbonate species irrespective of the environmental conditions, while acetate oxidation is more favorable with uranyl hydroxide species when U(VI) > 0.5 μM in these conditions. These findings suggest that the bioavailable U(VI) species is likely the same for both *Shewanella* and *Geobacter*.

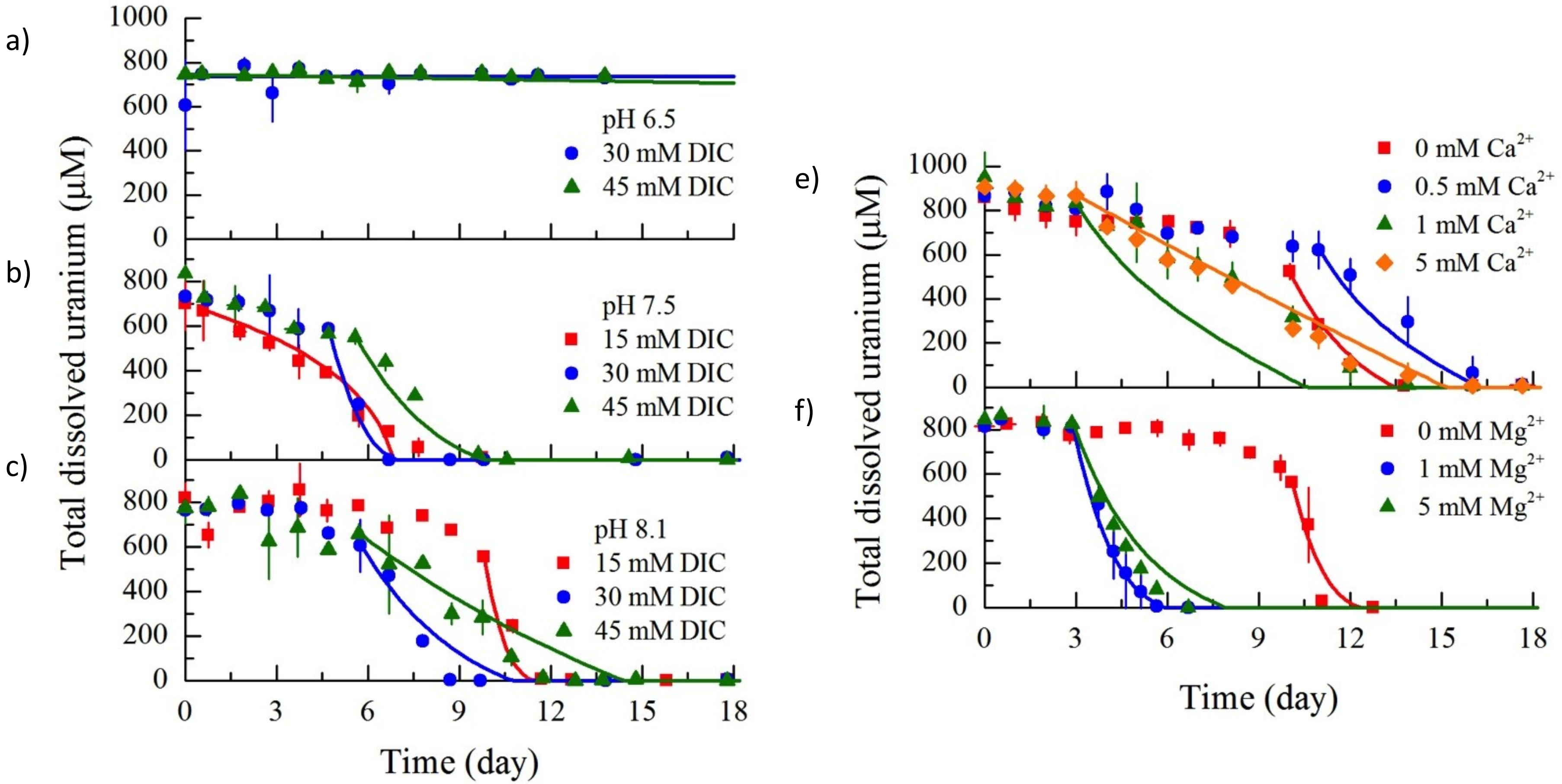

Figure 3. Averaged, time-corrected total dissolved uranium concentration time series in duplicate bioreduction incubations conducted without added Ca^{2+} and Mg^{2+} at pH (a) 6.5, (b) 7.5, and (c) 8.1 in the presence of various concentrations of DIC, and amended with various concentrations of (d) Ca^{2+}; and (e) Mg^{2+} at pH 8.1 in the presence of a constant DIC concentration. Symbols represent measured values and solid lines represent optimized model outputs. Error bars represent duplicate incubations. These incubations reveal that the reduction of U(VI) is strongly influenced by the pH, concentration of carbonates, and the hardness of the medium.

a)

Uranyl species	**Rate constant (L/cell/day)**
Non-carbonate	3.42 (±1.61) x 10^{-6}
Carbonate	5.40(±1.61) x 10^{-12}
Ternary carbonate	1.37(±0.28) x 10^{-12}

b)

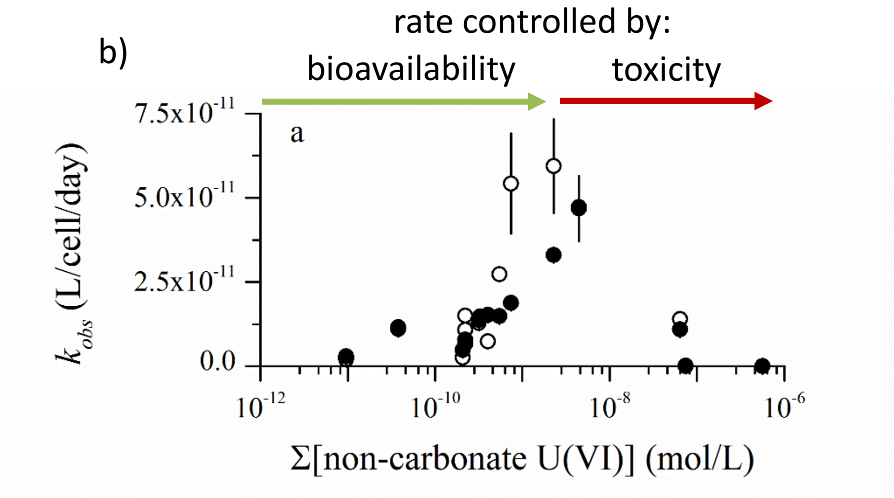

Figure 4. a) Optimized rate constants for the speciation-dependent U(VI) bioreduction rate law optimized using the entire data set shown in Figure 3. Rate constants were partitioned in non-carbonate U(VI) complexes, including the ‘free’ uranyl ion, hydroxide complexes, and other minor complexes, U(VI) carbonate complexes, and ternary Ca and Mg U(VI) carbonate complexes. Optimization of these three classes of rate constants demonstrate that the bioavailability of the non-carbonate species is much higher than the carbonate or ternary carbonate complexes. b) Overall pseudo first-order rate constant of U(VI) bioreduction as a function of the concentration of non-carbonate U(VI) species. This relationship illustrates that the bioavailability of U(VI) increases as the concentration non-carbon U(VI) complexes increases to a maximum U(VI) bioreduction rate, then decreases as the concentration of non-carbonate U(VI) complexes is toxic to the cells (Belli et al., 2015).

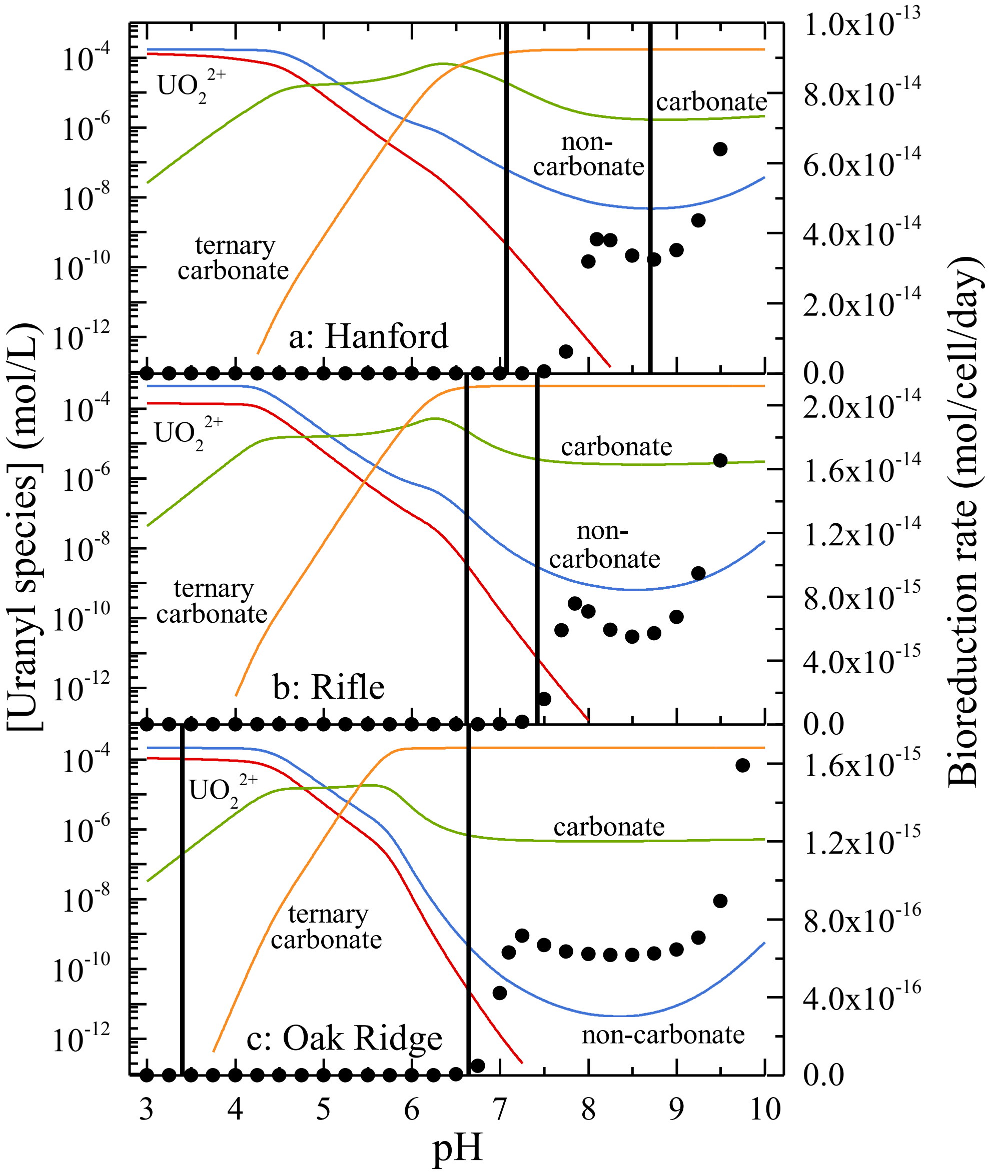

Figure 5. Calculated aqueous uranyl speciation (lines) and bioreduction rate (black symbols) as a function of pH using background groundwater composition at the (a) Hanford, (b) Rifle, and (c) Oak Ridge US Department of Energy (DOE) Integrated Field Research Challenge (IFRC) sites, assuming a 3 mM acetate injection to stimulate metal-reducing bacteria. Solid vertical lines represent the minimum and maximum measured pH at each site. Bioreduction rates were calculated using the proposed biogeochemical kinetic model and the optimized model parameters (Belli et al., 2015).

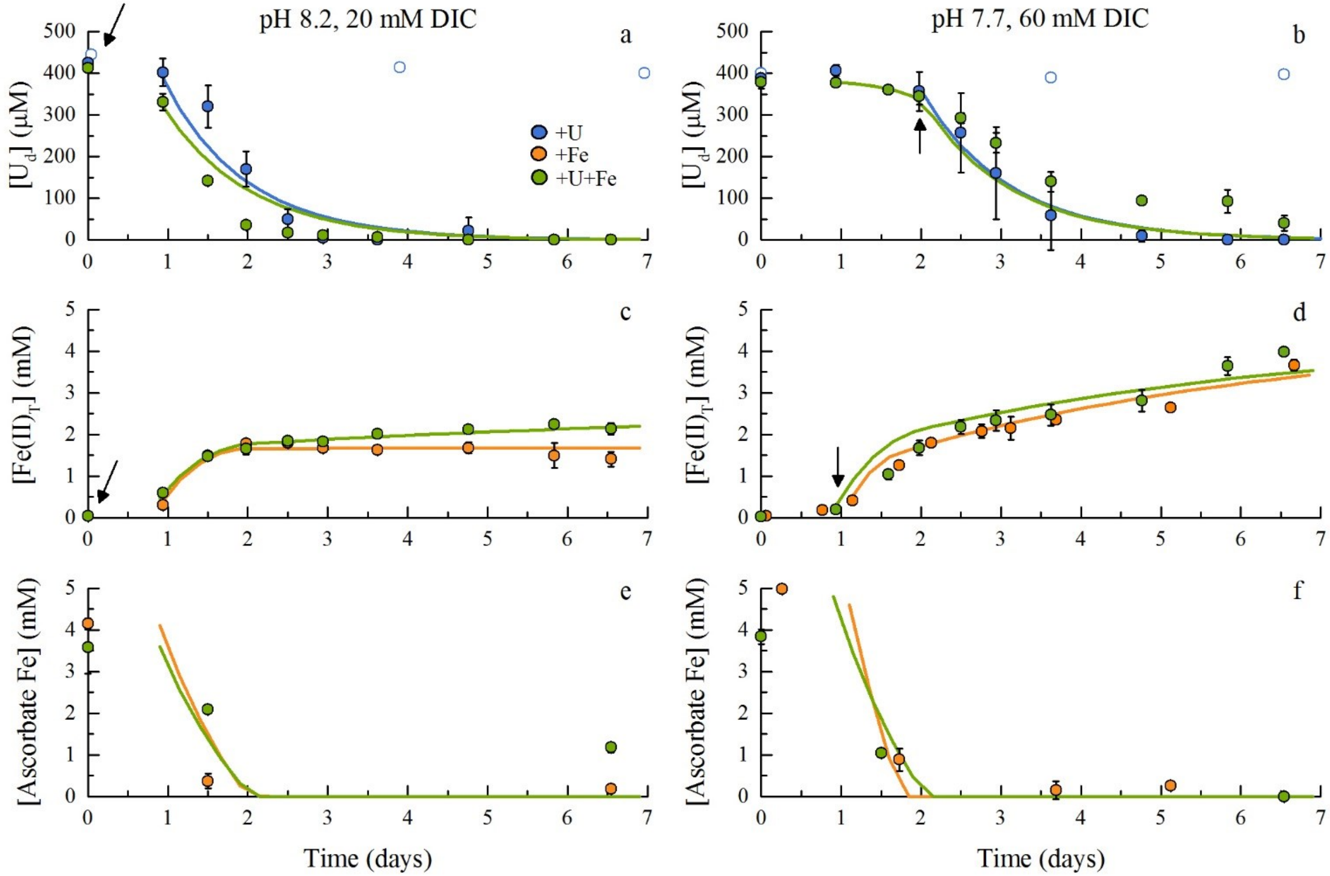

Figure 6. Time series of (a and b) total dissolved uranium (U_d), (c and d) total Fe(II) ($Fe(II)_T$), and (e and f) ascorbate-extractable solid-phase iron in bioreduction incubations with *S. putrefaciens* amended with U(VI) (+U, blue), 2-line ferrihydrite (+Fe, orange), or both (+U+Fe, green) as TEAs under two geochemical conditions: pH 8.2, 20 mM DIC (left) and pH 7.7, 60 mM DIC (right). Abiotic controls for the uranium-only treatment are shown in open symbols (a and b). 15 mM lactate was provided as the electron donor in all incubations. Symbols represent measured values, and lines represent the output of an optimized kinetic model that uses bioenergetics to reproduce the evolution of U(VI) and Fe(II) during the anaerobic respiration of Fe(III) oxides and/or U(VI) by *S. putrefaciens*. Arrows indicate the onset of (a and b) uranium removal or (c and d) Fe(II) production in the +U+Fe treatments (green). Error bars reflect the standard deviation of measured concentrations from duplicate incubations

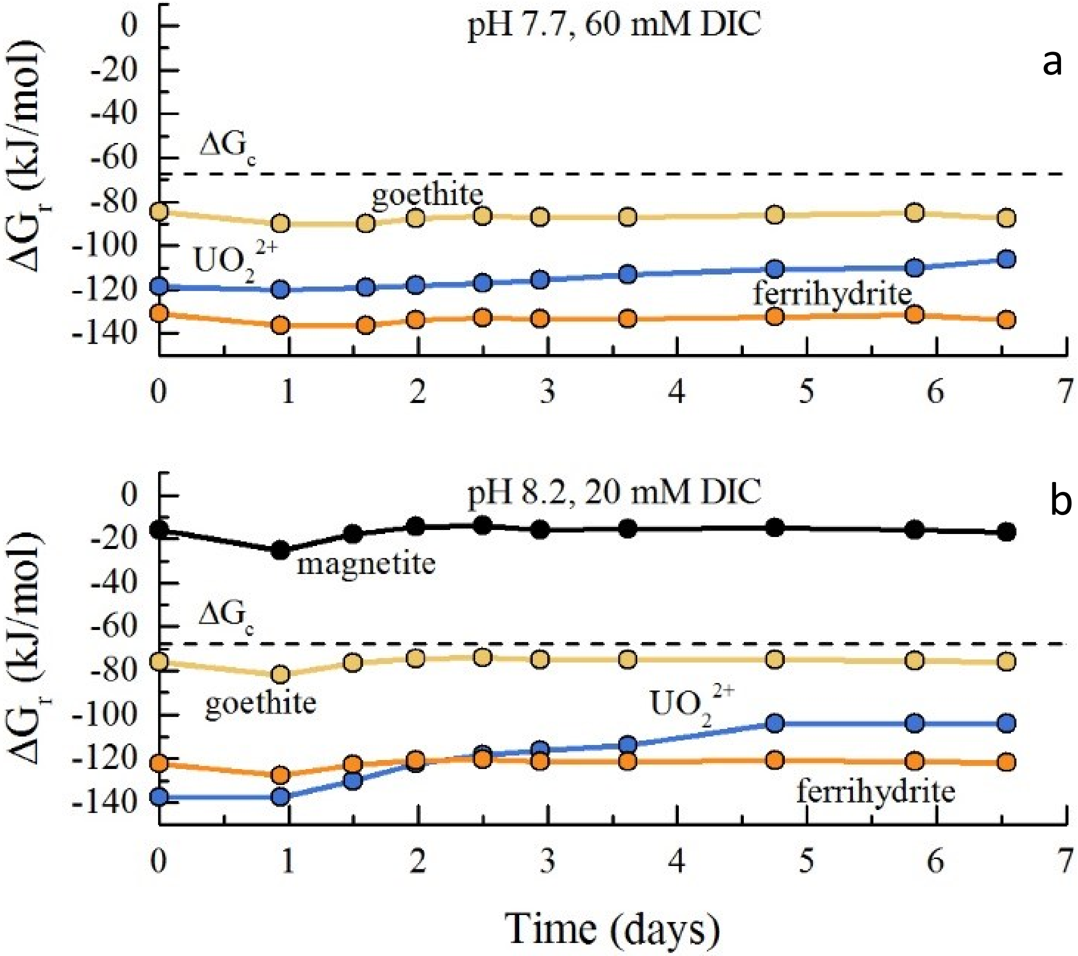

Figure 7. Time series of ΔG_r for the oxidation of lactate coupled to the reduction of UO_2^{2+} (blue), 2-line ferrihydrite (orange), goethite (yellow), and magnetite (black) over the course of the bioreduction incubations with *S. putrefaciens* at: a) pH 8.2 in the presence of 20 mM DIC; and b) pH 7.7 in the presence of 60 mM DIC. The dashed line represents the Gibbs energy conserved by *S. putrefaciens* (ΔG_C, -67.5 kJ/mol), the minimium energy that must be available for the respiration reaction to proceed. These data reveal that at pH 7.7, ferrihydrite is always favorable

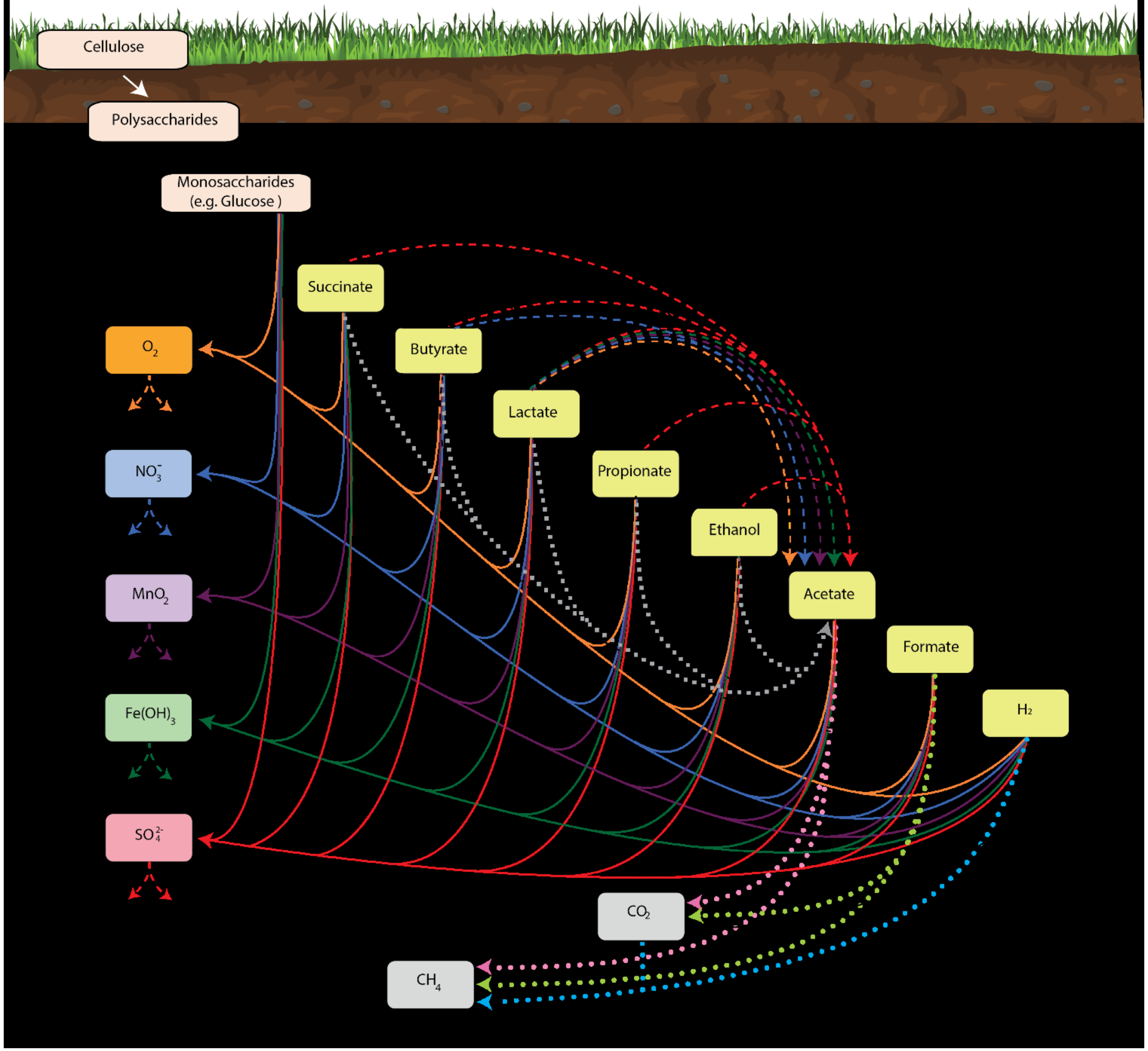

Figure 8. Conceptual model for microbial organic matter degradation. Solid black lines (──) refer to major glucose fermentation products. Black dashed lines (‒ ‒) denote single secondary fermentation pathways, while gray dashed lines (- - -) refer to fermentation pathways leading to acetate formation. Coloured solid lines illustrate the major heterotrophic respiration pathways leading from the electron donor (yellow box) to the corresponding electron acceptor. Coloured dashed lines refer to heterotrophic respiration products including inorganic products (left side) and organic products (upper right). Dotted lines refer to methanogenic pathways: (····) acetoclastic, (····) hydrogenotrophic and (···) formate.

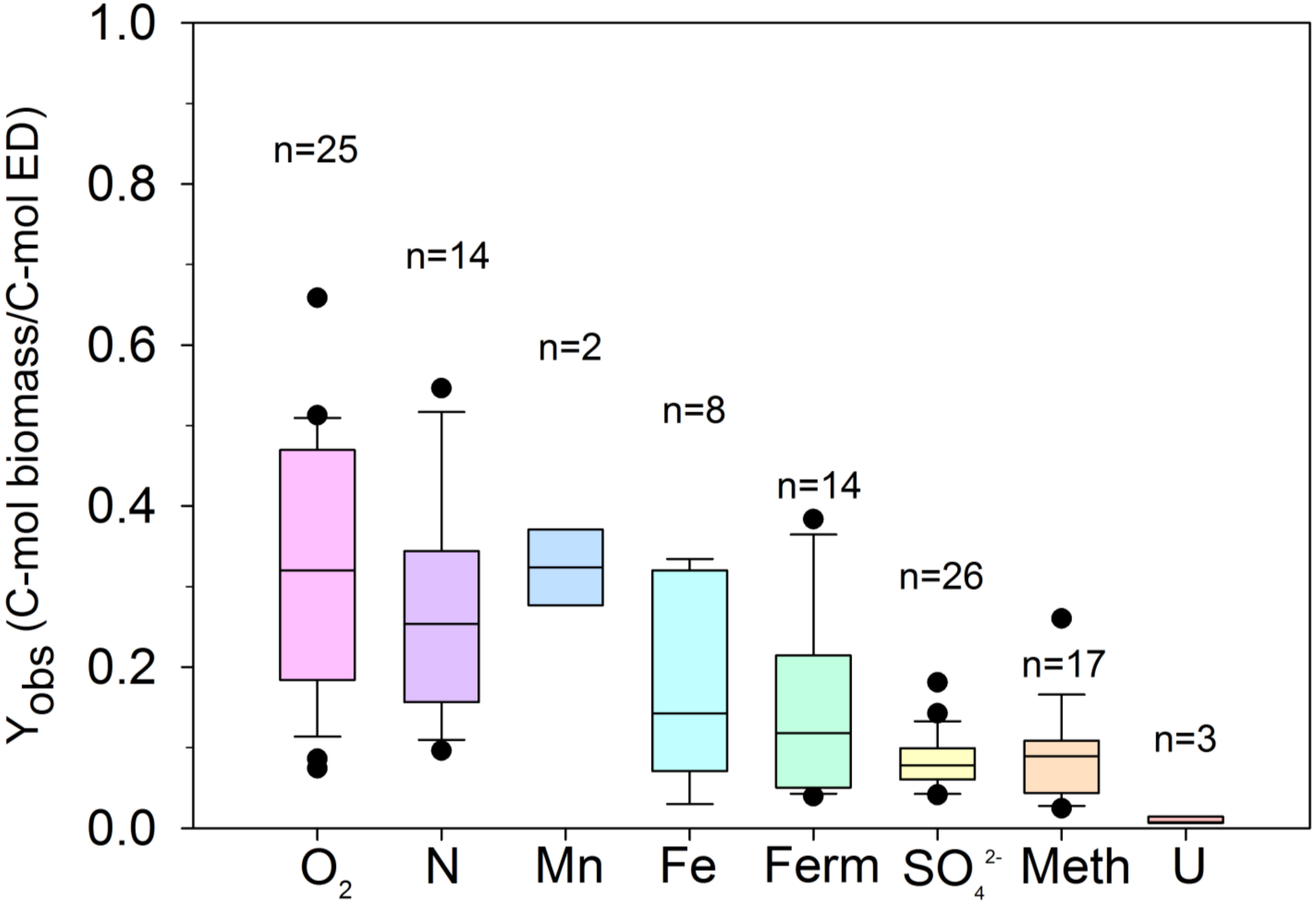

Figure 9. Compiled literature values of A) observed Y for the major electron accepting and fermentation (Ferm) and methanogenic (Meth) metabolic pathways whereby the black circles represent outliers. N refers to denitrification and dissimilatory nitrate reduction to ammonium (DNRA) pathways. Note: all literature values reported as per mol H_2 are omitted from the plot.

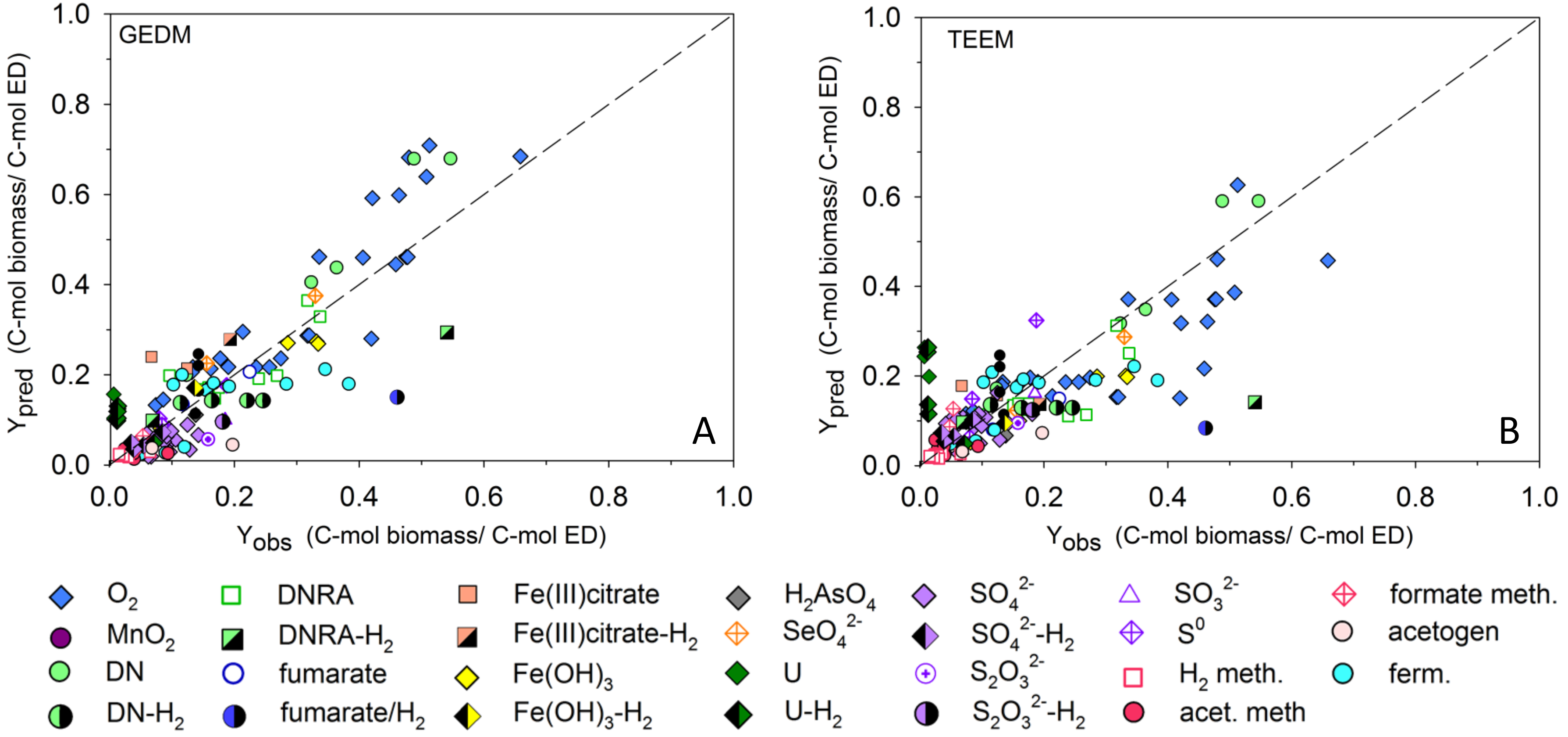

Figure 10. Parity plots of observed growth yields (Y) versus predicted static growth yields (Y^{pred}) using A) TEEM and B) GEDM of the major electron accepting and fermentation (Ferm) and methanogenic (Meth) metabolic pathways. DN and DNRA and represents denitrification and dissimilatory nitrate reduction to ammonium, respectively. The dashed black line represents the 1:1 prediction line. All Y values are expressed at C-mol biomass/C-mol C source except for those denoted with an H_2 which are expressed as C-mol biomass/mol H_2. Note the deviation of Y values from the parity line for U reduction (denoted by dark green diamond) from the 1:1 line.

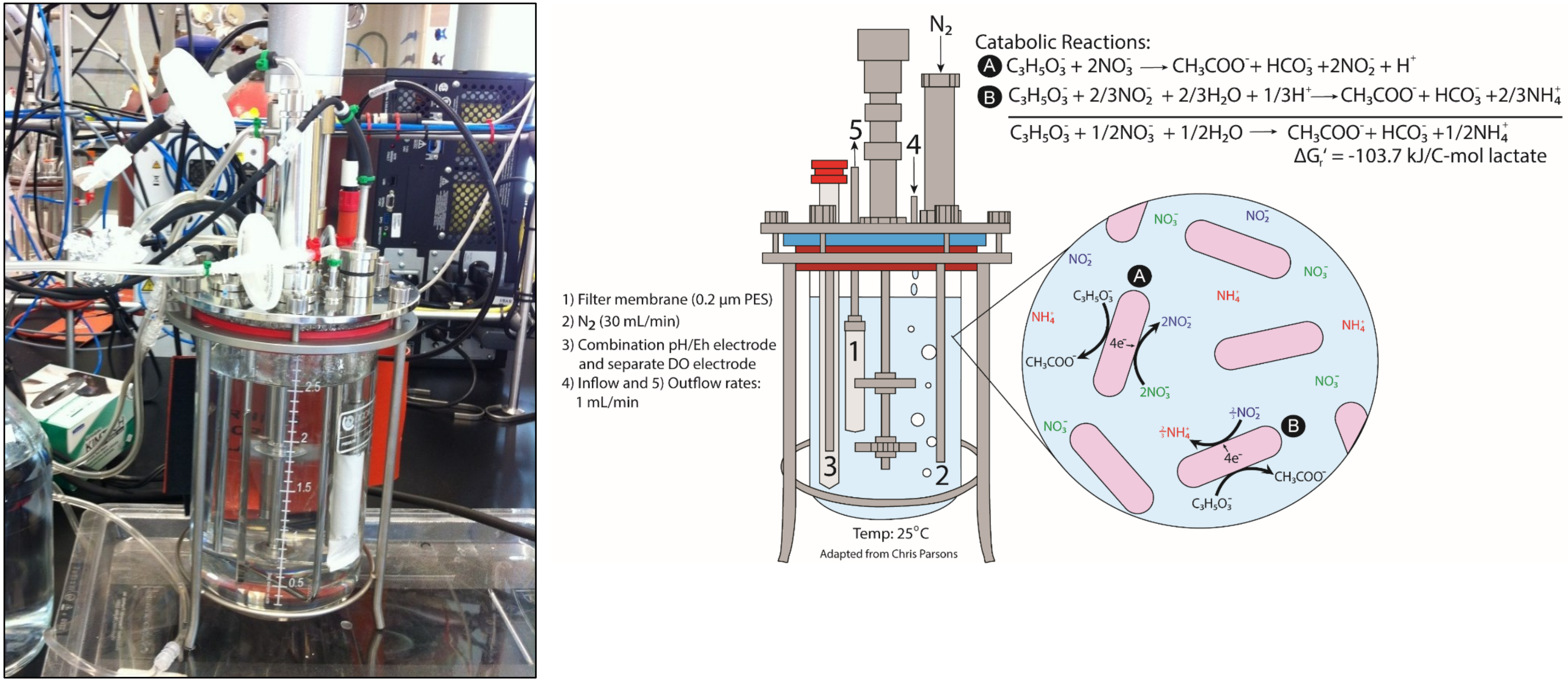

Catabolic Reactions:

$$\text{A}\quad C_3H_5O_3^- + 2NO_3^- \longrightarrow CH_3COO^- + HCO_3^- + 2NO_2^- + H^+$$

$$\text{B}\quad C_3H_5O_3^- + 2/3NO_2^- + 2/3H_2O + 1/3H^+ \longrightarrow CH_3COO^- + HCO_3^- + 2/3NH_4^+$$

$$C_3H_5O_3^- + 1/2NO_3^- + 1/2H_2O \longrightarrow CH_3COO^- + HCO_3^- + 1/2NH_4^+$$

$$\Delta G_r{}' = -103.7 \text{ kJ/C-mol lactate}$$

1) Filter membrane (0.2 µm PES)
2) N_2 (30 mL/min)
3) Combination pH/Eh electrode and separate DO electrode
4) Inflow and 5) Outflow rates: 1 mL/min

Temp: 25°C

Adapted from Chris Parsons

Figure 11. Retentostat set up and schematic: Catabolic energy was gained from the reduction of NO_3^- to NH_4^+.

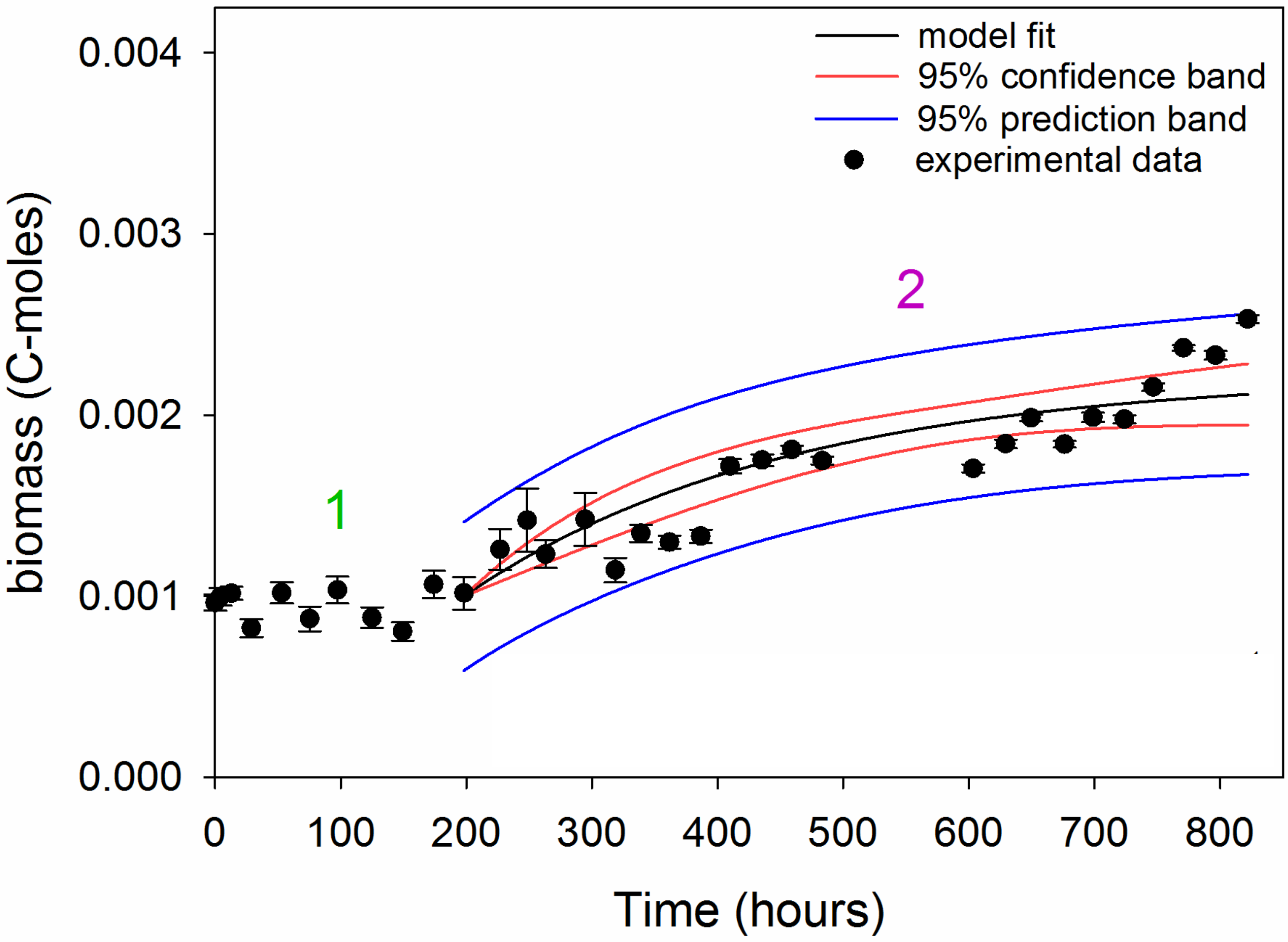

Figure 12. Biomass concentrations and lag (1) and growth (2) phases of the retentostat biomass data.

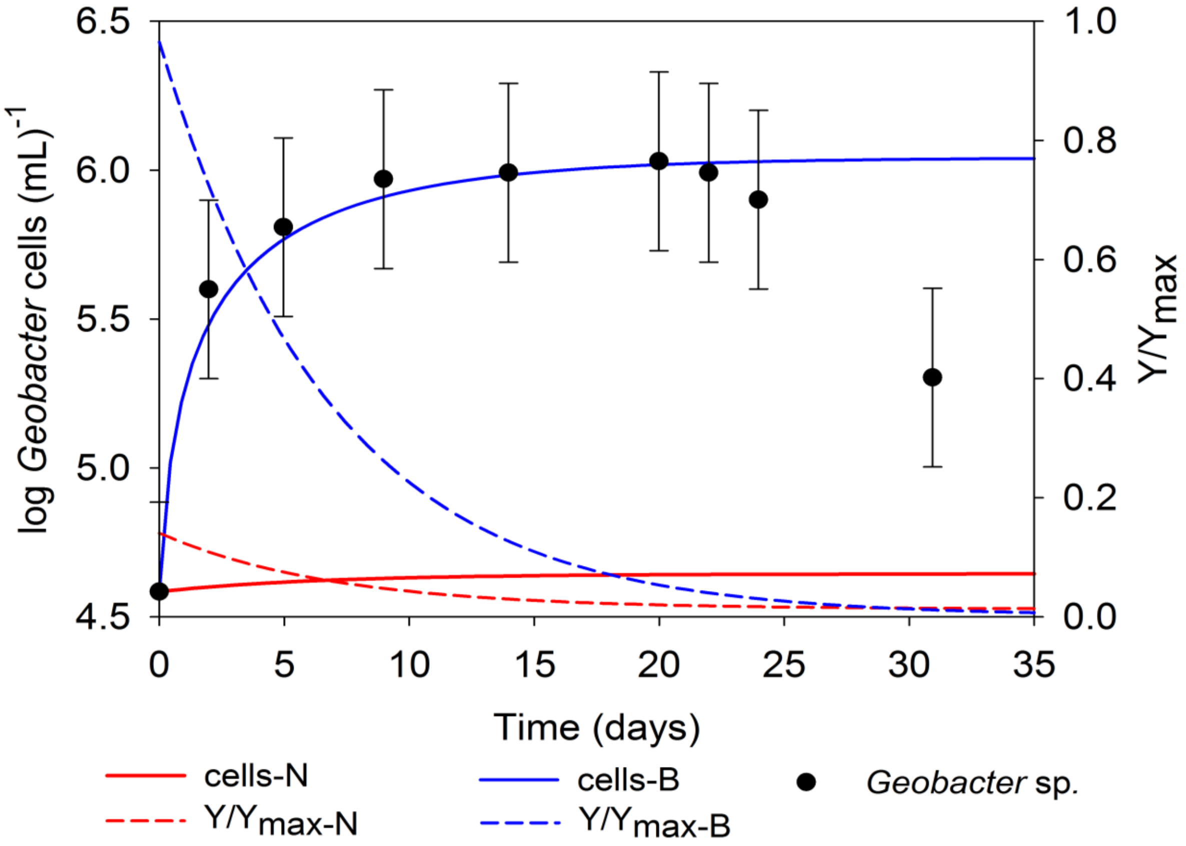

Figure 13. Published *Geobacter* sp. cell counts from Holmes et al., (2013) and predicted cell numbers with the corresponding Y/Y_{max} based on natural (N) and biostimulated (B) conditions at the Rifle Field Site predicted using a bioenergetics-based dynamic growth yield model. Note the good agreement between cell numbers measured (black circles) and predicted (blue solid line) during the biostimulation event. Moreover, the results demonstrate that at highest growth rate the observed growth yields under natural conditions only comprised 15% of the maximum growth yield predicted thereby highlighting the importance of implementing dynamic growth yields in microbial growth models.